Mesoscopic Klein-Schwinger effect in graphene

Aurélien Schmitt, Pierre Vallet, Michael Rosticher, Takashi Taniguchi, Kanji Watanabe, Erwann Bocquillon, Gwendal Fève, Jean-Marc Berroir, Christophe Voisin, Jérôme Cayssol, et al.

Mesoscopic Klein-Schwinger effect in graphene

A. Schmitt,[1,*] P. Vallet,[2] D. Mele,[1,3] M. Rosticher,[1] T. Taniguchi,[4] K. Watanabe,[4] E. Bocquillon,[1,5] G. Fève,[1] J.M. Berroir,[1] C. Voisin,[1] J. Cayssol,[2] M. O. Goerbig,[6] J. Troost,[1] E. Baudin,[1,†] and B. Plaçais[1,‡]

[1]*Laboratoire de Physique de l'Ecole normale supérieure, ENS, Université PSL, CNRS, Sorbonne Université, Université de Paris, 24 rue Lhomond, 75005 Paris, France*

[2]*Laboratoire Ondes et Matière d'Aquitaine, 351 cours de la libération, 33405 Talence, France*

[3]*Univ. Lille, CNRS, Centrale Lille, Univ. Polytechnique Hauts-de-France, Junia-ISEN, UMR 8520-IEMN, F-59000 Lille, France.*

[4]*Advanced Materials Laboratory, National Institute for Materials Science, Tsukuba, Ibaraki 305-0047, Japan*

[5]*II. Physikalisches Institut, Universität zu Köln, Zülpicher Strasse 77, 50937 Köln*

[6]*Laboratoire de Physique des Solides, CNRS UMR 8502, Univ. Paris-Sud, Université Paris-Saclay, F-91405 Orsay Cedex, France*

Abstract

Strong electric field annihilation by particle-antiparticle pair creation, described in detail by Sauter and Schwinger, is a basic non-perturbative prediction of quantum electrodynamics. Its experimental demonstration remains elusive as Schwinger fields E_S are beyond reach even for the light electron-positron pairs. Here we put forward a mesoscopic variant of the Schwinger effect in graphene, which hosts Dirac fermions with electron-hole symmetry. Using DC transport and RF noise, we report on universal 1d-Schwinger conductance at the pinch-off of ballistic graphene transistors. Strong pinch-off electric fields are concentrated in a length $\Lambda \gtrsim 0.1\ \mu\mathrm{m}$ at the transistor drain, and induce Schwinger e-h pair creation at saturation, for a Schwinger voltage $V_S = E_S\Lambda$ on the order of the pinch-off voltage. This Klein-Schwinger effect (KSE) precedes an instability toward an ohmic Zener regime, which is rejected at twice the pinch-off voltage in long devices. The KSE not only gives clues to current saturation limits in ballistic graphene, but also opens new routes for quantum electrodynamic experiments in the laboratory.

A variety of important physical phenomena requires a non-perturbative understanding of quantum field theory. This includes solitonic waves, but also several crucially quantum mechanical phenomena like the confinement of quarks in quantum chromodynamics. While many non-perturbative problems are notably hard to compute, some are within reach and yield accurate predictions. Among the most striking non-perturbative predictions of quantum field theory is the instability of an electric field under the creation of massive charge carriers. The Schwinger effect (SE) states that pairs are created, out of a false vacuum with an electric field, to diminish the energy of the state. It is a simple yet non-trivial and non-perturbative prediction of quantum electrodynamics [1–4]. The pair-creation rate per unit d-dimensional volume reads $w(E) \propto \sum_{n\geq 1} \left(\frac{E}{n}\right)^{\frac{d+1}{2}} e^{-\pi \frac{nE_S}{E}}$ (see prefactors in [4] and Supplementary Section-I), where E is the electric field and $E_S = \Delta_S^2/e\hbar c = 1.32\ 10^{18}$ Vm^{-1}, called Schwinger field, corresponds to the electron-mass energy $\Delta_S = mc^2 = 511$ keV needed to create an electron-positron pair at a characteristic length-scale given by the Compton length $\lambda_C = hc/\Delta_S$. Large efforts have been devoted to produce such extremely strong electric fields in the laboratory to check this prediction explicitly [5]. Unfortunately, the attempts to observe SE in the last decades have not yet been met with success.

With the advent of graphene, a novel playground for the study of relativistic effects has been opened in the completely different framework of condensed matter physics [6–10]. In such a mesoscopic variant, electron-positron pairs are substituted by electron-hole pairs, speed of light c by the Fermi velocity $v_F \simeq 10^6$ m/s, the rest energy by a bandgap $\Delta_S \lesssim 0.2$ eV (see below), leading to experimentally accessible Schwinger fields $E_S = \frac{\Delta_S^2}{e\hbar v_F} \lesssim 6.10^7$ Vm^{-1}. Neutral single layer graphene, considered in Refs.[8–10], corresponds to the gapless 2d limit where $E_S = 0$ so that the 2d-Schwinger rate reduces to a super-linear $J \propto E^{\frac{3}{2}}$ current-field relation, as observed in single layer graphene [12]. More recently, the same dependence has been reported in twisted bilayer graphene heterostructures, where the SE develops on top of a saturation current [13]. Our experiment is motivated by the study of transport in bottom gated (gate voltage V_g) single layer graphene field-effect transistors, where pair creation is subject to a finite breakdown field at large doping. Most saliently, our experiment investigates the large bias regime where Klein collimation establishes a quasi-one dimensional transport characterized by a transport gap Δ_S, and where the Schwinger effect is accurately fitted by the 1d pair-creation rate. Klein collimation develops over a ballistic junction, of length $\Lambda < 1$ μm, which builds up at current saturation when drain doping

is suppressed below the channel doping (density n_s) according to the drain-gate voltage $V \sim V_g$. It generates a peak effect with a large local electric field prone to the ignition of Schwinger-pair creation. As this situation differs from the canonical vacuum breakdown, we distinctively call it the Klein-Schwinger effect (KSE).

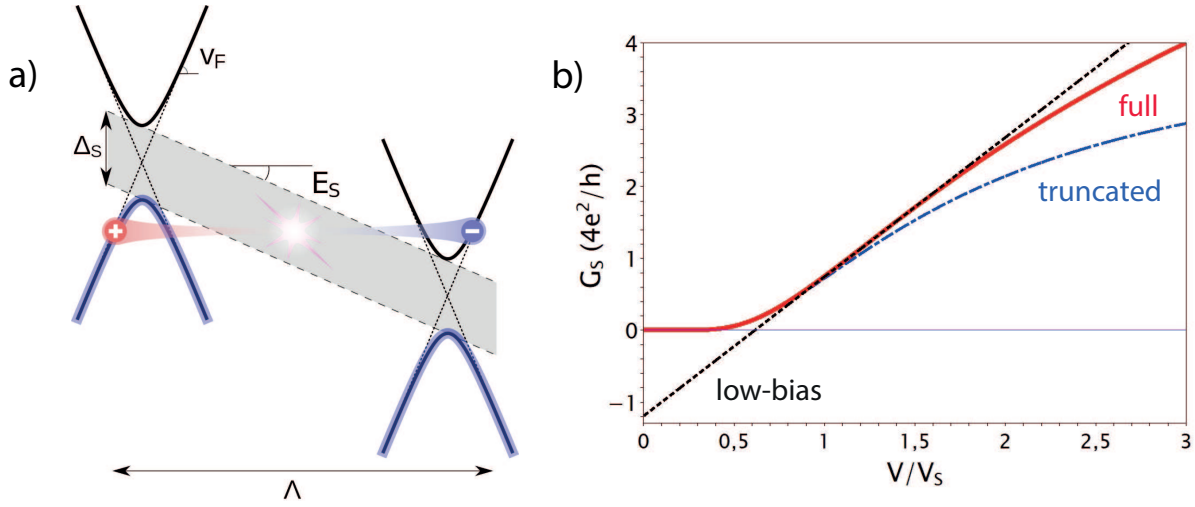

FIG. 1: Mesoscopic Schwinger effect for massive 1d-Dirac fermions. Panel a: Sketch of the 1d-Schwinger effect across a graphene junction of length Λ and gap $\Delta_S = m^* v_F^2$, defining a Schwinger field $E_S = \Delta_S^2/e\hbar v_F$ and a junction Schwinger voltage $V_S = E_S\Lambda$. It leads to the proliferation of electron-hole pairs at a rate $w_{1d}\Lambda$, with w_{1d} given by Eq.(1) and a pair-current given by Eq.(2). Panel b: the differential conductance $G_S = \partial I_S/\partial V$ given by Eq.(3) for $g_s = g_v = 2$ (red line). It is well approximated by the low-bias development (4), $G_S = 1.20\left(\frac{V}{V_C} - 1\right) \times \frac{4e^2}{h}$, with $V_C = 0.62V_S$ (black dashed line). The truncated Schwinger conductance (blue dash-dotted line), $G_S^* = 4g_s g_v \frac{e^2}{h}\left(1 + \pi\frac{V_S}{V}\right) e^{-\pi\frac{V_S}{V}}$ (see main text), significantly deviates from the full series (3).

Let us detail theoretical prediction for the mesoscopic 1d-Schwinger effect, as sketched in Fig.1-a. Pair creation is monitored by the current generated across the junction upon dissociation in the large electric field. Starting from the 1d-Schwinger rate, and taking into account spin and valley degeneracies g_s and g_v, the pair current I_S and differential

conductance G_S can be written as :

$$w_{1d} = \frac{2e}{h} E \sum_{n=1}^{\infty} \frac{e^{-n\pi \frac{E_S}{E}}}{n} \tag{1}$$

$$I_S = 4V \ln\left(\frac{1}{1-e^{-\pi\frac{V_S}{V}}}\right) \times g_s g_v \frac{e^2}{h} \qquad \text{with} \qquad V_S = \Lambda \frac{\Delta_S^2}{e\hbar v_F} \tag{2}$$

$$G_S = 4\left[\frac{\pi\frac{V_S}{V}}{e^{\pi\frac{V_S}{V}}-1} + \ln\left(\frac{1}{1-e^{-\pi\frac{V_S}{V}}}\right)\right] \times g_s g_v \frac{e^2}{h} \tag{3}$$

$$\approx 1.20\left(\frac{V}{V_C}-1\right) \times g_s g_v \frac{e^2}{h} \qquad (V_C = 0.62V_S \lesssim V \lesssim 2V_S) \tag{4}$$

where V is the total bias and V_S the Schwinger voltage, product of the Schwinger field $E_S = \frac{\Delta_S^2}{e\hbar v_F}$ by the length Λ of the pair-creation domain. The differential conductance (3) possesses an inflection point at $V = 1.22V_S$, with a tangent given by Eq.(4) and characterized by a critical voltage $V_C = 0.62V_S$ and a zero-bias extrapolate $-G_0$ with $G_0 = 1.20 g_s g_v \frac{e^2}{h}$. The Schwinger conductance (3) is plotted in Fig.1-b for 1d-graphene where $g_s = g_v = 2$ (solid red line), including the low-bias development (dotted black line for Eq.(4)) with $G_0 = 0.186$ mS. Also shown in the figure is the conductance $G_S^* = 4 g_s g_v \frac{e^2}{h}\left(1+\pi\frac{V_S}{V}\right) e^{-\pi\frac{V_S}{V}}$ (dash-dotted blue line) calculated with the Schwinger rate (1) truncated to its first $n = 1$ term; the truncated variant deviates from the full Schwinger conductance for $V/V_S \gtrsim 1.5$ and $G_S \gtrsim 0.2$ mS. Comparison of massive 1d and 2d-Schwinger conductances, as well as that of 3d-Schwinger and the non relativistic Fowler-Nordheim mechanism, are discussed in Supplementary Section-I.

Measurements are performed at room temperature in a series of 6 hBN-encapsulated single-layer-graphene transistors deposited on local back-gates, made of graphite for devices GrS1-3 and Au for devices AuS1-3, and equipped with high-transparency edge contacts (see Methods and Supplementary Section Table-I). As explained in Section I, high-mobilities $\mu \gtrsim 10$ m^{2}V^{-1}s^{-1}, large dimensions $(L, W) \gtrsim 10$ μm, high doping n_s and small gate-dielectric thicknesses $t_{hBN} \lesssim 100$ nm, are key ingredients for observing the Schwinger effect. High mobility provides current saturation at low bias $V_{sat} < V_g$, whereas high-doping and long channels are needed to reject the Zener channel instability at a large bias $V_Z > V_g$. The Schwinger effect is visible in the $[V_{sat}, V_Z]$ window at a Schwinger voltage $V_S \sim V_g$ controlled by the channel doping n_s and dielectric thickness t_{hBN}. Data reported below refer mostly to the representative GrS3 sample, leaving the full sample series description for the Supplementary Section-IV.

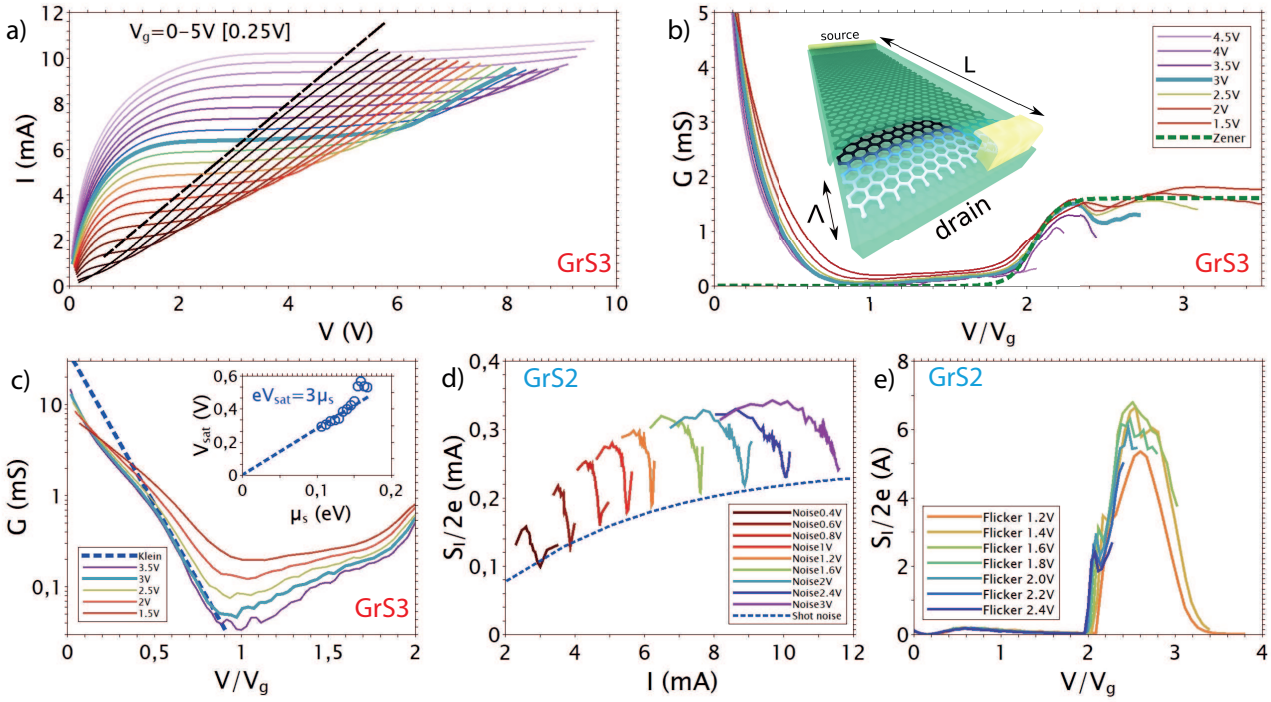

FIG. 2: Room temperature ballistic pinch-off in sample GrS3 of dimensions $L\times W\times t_{hBN} = 15\times 10\times 0.042$ μm, mobility $\mu = 12\mathrm{m}^2\mathrm{V}^{-1}\mathrm{s}^{-1}$ (gate capacitance $C_g = 0.67\mathrm{mFm}^{-2}$), and contact resistance $R_c = 120\Omega$. Panel-a: Set of current-voltage characteristics after subtraction of contact voltage drop, including the representative $V_g = 3$ V trace (thick turquoise line). The pinch-off regime $V = V_g$ is indicated by the dashed black line. Panel-b: differential conductance scaling $G\left[\frac{V}{V_g}\right]$ illustrating the steep decay of saturation conductance below pinch-off, and the sharp onset of Zener conductance at twice the pinch-off voltage. Inset is an artist view of the supposed carrier density distribution, characterized by a sharp drop over a collimation length Λ at the drain side. Panel-c: semi-log representation of conductance showing the exponential decay at current saturation, $G = G(0)e^{-\frac{V}{V_{sat}}}$ (dotted blue line), with a doping dependent saturation voltage $V_{sat} \simeq 3\mu_s/e$ (dashed line in the inset). Panel-d: High-frequency (1–10 GHz) current noise measured in sample GrS2 at $T = 10$ K as function of current. The sharp drop at pinch-off maps the vanishing of the thermal noise contribution $S_I = 4G(I)k_BT_e$, where T_e is the hot-electron temperature, according to the differential conductance dip at saturation. The residual noise (dashed blue line) is attributed to shot noise $S_I = 2eIF$ obeying the Fano factor $F \simeq 0.04/\sqrt{1+(I_{sat}/0.006)^2}$.

I. KLEIN COLLIMATION JUNCTION

Prior to discussing Schwinger effect in Section II, it is worth understanding the current saturation mechanism which creates the electric field profile it stems from. We show in Fig.2-a the high-bias transport characteristics of sample GrS3 (details in the caption of Fig.2), which exhibit prominent current saturation plateaus centered at the $I(V = V_g)$ pinch-off line (dashed black line). We have highlighted the representative $V_g = 3$V trace (thick turquoise line) that illustrates the three main transport regimes: i) the diffusive Drude regime for $V \lesssim V_{sat}$, ii) the saturation regime for $V_{sat} \lesssim V \lesssim V_Z$, and iii) the Zener regime for $V \gtrsim V_Z$. As discussed in previous works [14,15], the Zener effect corresponds to a field-induced inter-band Klein tunneling and is characterized by a doping-independent Zener channel conductivity ($\sigma_Z \sim 1$ mS). The Zener effect is subject to Pauli blockade leading to a finite threshold voltage $V_Z = LE_Z$ with a critical field $E_Z \propto \mu_s^2 \propto n_s$, where μ_s is the channel doping energy [15]. Consequently the Zener voltage $V_Z \propto LV_g$ of long transistors is rejected well above V_g. This important feature characterizes our device series (see Supplementary Section-IV), which differs from conventional devices [16,17] where lower mobility and shorter channel lengths substitute saturation plateaus by a crossover between the Drude and Zener ohmic regimes. Remarkably, in spite of their large channel lengths, our high-mobility devices sustain large saturation velocities ($I/n_seW \simeq 0.3v_F$ in Fig.2-a).

Current saturation is best characterized by the differential conductance $G = \partial I/\partial V$, whose scaling properties as function of V/V_g are shown in Fig.2-b. The figure is a close-up on the saturation and Zener regimes, cutting-off the Drude regime which corresponds to larger conductances $G_{Drude} \simeq$ 10–40 mS. The high-bias Zener regime corresponds to a doping-independent step-like increase to $G_Z \simeq 1.5$ mS ($\sigma_Z \simeq 2$ mS) at $V_Z \simeq 1.8V_g$. The saturation regime of interest in this work is characterized by a vanishing conductance in the $[V_g, V_Z]$ window.

To account for this conductance suppression we propose a Klein-collimation-junction interpretation, as sketched in the inset of Fig.2-b. It relies on the small Drude voltage drop $\Delta V_{Drude} = I/G_{Drude} \lesssim 0.2$ V along the main part of the channel length, which prevents the ignition of inelastic scattering mechanisms (see Ref.[14]) and secures large drift velocities; it entails a small bulk electric field ($\lesssim 10^4$ Vm^{-1}) and a quasi uniform channel doping. As a consequence, the voltage drop is confined in a small junction (length Λ) at the tran-

sistor drain end, generating an electrical peak effect reaching the large local electric fields $V/\Lambda \sim 5.10^7$ Vm^{-1} needed to trigger the mesoscopic Schwinger effect. Importantly, these fields remain one order of magnitude smaller than the breakdown field of the hBN dielectric [18]. This peak effect is the semi-metal variant of the channel pinch-off of metal-oxide-semiconductor field-effect transistors (MOSFETs) [19]. The Klein-collimation-junction interpretation of saturation is supported by a detailed conductance analysis (panel c) and two additional noise characterizations (panels d and e) discussed below.

Fig.2-c is a semi-log plot showing the exponential decay of the saturation conductance below the pinch-off voltage V_g. It is exemplified by the dashed-blue-line fit of the representative $V_g = 3V$ data. This exponential decay is observed over a broad doping range, and characterized by a doping-dependent saturation voltage V_{sat} according to the fitting law $G = G(0)e^{-V/V_{sat}}$. The inset shows the Fermi-energy dependence of V_{sat} which obeys a linear law $V_{sat} \simeq 3\mu_s/e$, implying that intra-band conductance suppression at pinch-off, $G(V_g \propto \mu_s^2) \propto e^{-\mu_s/Cte}$, increases with doping. This property is consistently observed in the full sample series (table SI-1) where $eV_{sat}/\mu_s = 2.5$–5. The exponential suppression of conductance is reminiscent of that of the transmission of a smooth graphene p-n junction $T(\varepsilon,\theta) \sim \exp -\pi\frac{|\varepsilon|}{\varepsilon_\Lambda}\sin^2\theta$ as function of energy ε [20], where $\varepsilon_\Lambda = \hbar v_F/\Lambda$ is the characteristic energy scale of the junction of length Λ, and θ the impinging-electron incidence angle. This expression illustrates how an in-plane electric field collimates electrons within a small angular aperture $\theta_c = \arcsin\sqrt{\varepsilon_\Lambda/|\varepsilon|}$, which is known as the Klein collimation effect. In a gate-defined p-n junction, which corresponds to an equilibrium situation where $\varepsilon = \mu_s$, Λ is set by the gate spacing [20,21]. In our bias-defined Klein-junction, which corresponds to a strongly out-of-equilibrium regime where $|\varepsilon| = eV - \mu_s \gg \mu_s$, we have $\Lambda \gtrsim t_{hBN}$ as the only length-scale of the device. The bias-induced Klein collimation effect turns an incident 2d electron gas into a 1d transmitted beam, leading to an emergent 1d transport regime.

A second signature of the existence of a Klein junction is found in the transistor shot noise in Fig.2-d. Shot noise $S_I = 2eI\mathcal{F}$, where $\mathcal{F} \lesssim 1$ is the Fano factor, is deduced from the microwave current noise S_I, which adds to the thermal noise $S_I = 4G(I)k_BT_e$ where T_e is the electronic temperature. Here we take advantage of the conductance suppression at saturation, with $G(I \simeq I_{sat}) \to 0$ corresponding to the noise dips at the saturation current I_{sat} in Fig.2-d, to extract the junction Fano factor $\mathcal{F}(I_{sat}) \lesssim 0.04$ (see Supplementary Section-III). The presence of a shot noise, and the tiny value of the Fano factor, are strong indications

of the presence of a ballistic junction [22]. Finally, the Zener threshold is reached upon increasing further the bias voltage; it entails an upheaval of the electric field distribution, as the electric field, initially confined over Λ at saturation, penetrates the full channel length L in the ohmic Zener regime. A signature of this avalanche-like instability can be seen in the huge low-frequency current noise observed in the $[V_Z, 1.5V_Z]$ range in Fig.2-e.

The exponential current saturation, the presence of shot noise, and the Zener electric-field instability are independent signatures of the Klein collimation effect and of its breakdown by the bulk Zener effect. The associated electric peak effect will be the seat for the Schwinger effect demonstrated below.

II. THE KLEIN-SCHWINGER EFFECT

In order to highlight the small Schwinger-pair contribution in transport, we magnify in Fig.3-a the conductance-scaling plot of Fig.2-b. We focus first on the $V_g = 3$V data (turquoise circles), for which the exponential tails of the Klein collimation (dotted blue line) and Zener (dotted green line) contributions are fully suppressed in a bias window $[1.1V_g, 1.7V_g]$. In these conditions, the measured conductance is solely governed by the Schwinger-pair contribution, as evidenced by the fit of $V_g = 3$V-data with Eq.(3) taking $V_S = 1.4V_g$ (thick turquoise line). The Schwinger contribution is also visible at lower doping, albeit partially obscured by a residual Klein contribution due to a less efficient Klein collimation (see Section-I). In order to extract the Schwinger-contribution at arbitrary doping, we rely on the de-embedding of the intra-band Klein contribution using a three-parameter fit $G = G_S(V/V_S) + G(0)e^{-V/V_{sat}}$ performed in the $[V_{sat}, V_Z]$ range. The resulting pair conductance is displayed in Fig.3-b. It highlights the sharp transition (dotted black line) between the Schwinger and Zener regimes, and reveals the Schwinger-conductance fan-like scaling predicted by the low-bias expression (4) for a doping-dependent V_S. Remarkably, the linear zero-bias extrapolate is a constant $G_0 \simeq 0.18 \pm 0.02$ mS, which is very close to the universal quantization $G_0 = 1.20\frac{4e^2}{h} = 0.186$ mS for the 1d-Schwinger effect in graphene. The same procedure has been applied to the full sample series in Fig.SI-(6,7), which shows similar scaling with consistent values of G_0. This observation of a robust conductance quantization, in quantitative agreement with 1d-Schwinger theory, demonstrates the ubiquity of the Klein-Schwinger effect and the relevance of Schwinger theory.

Going one step further, we analyze the Schwinger-voltage doping dependencies deduced from theoretical fits of pair-conductance data with expression (3). Considering that $\Delta_S \propto \mu_s$ is the only energy scale in the problem, so that $E_S \propto \mu_s^2 \propto V_g$, we plot in Fig.3-c the ratio $V_S/V_g(n_s)$ for the full device series. We observe a linear doping dependence with a slope that increases with gate dielectric thickness $t_{hBN} = 25$–90nm. As detailed in the Supplementary Section-V, these dependencies can be explained by a doping dependence of the junction length Λ according to the law $\frac{\Lambda}{t_{hBN}}\frac{\Delta_S^2}{\mu_s^2} = 4\alpha_g \frac{V_S}{V_g}$, where $\alpha_g = \frac{e^2}{4\pi\epsilon_{hBN}\varepsilon_0\hbar v_F} = 0.70$ (with $\epsilon_{hBN} = 3.1$ at high field [18]) is the graphene fine structure constant. Assuming that $\Delta_S \simeq \mu_s$, we can cast the measured $\frac{V_S}{V_g}(t_{hBN}, n_s)$ into the t_{hBN} power expansion $\Lambda \simeq a t_{hBN} + \xi n_s t_{hBN}^2$. The doping-independent term $a = 1$–2 is consistent with a geometrical factor depending on the details of the contact-gate arrangements which is an a-posteriori justification of our $\Delta_S \simeq \mu_s$ Ansatz; the factor $\xi \simeq 4$ nm is a microscopic interaction length[30], quantifying the doping-induced dilation of the junction length. This Coulomb-repulsion effect enhances V_S, favoring the observation of the Klein-Schwinger effect at large doping (GrS3-data in Fig.3-c), up to the limit where its onset exceeds V_Z so that Schwinger effect becomes masked by the Zener instability (AuS3-data in Fig.3-c). The latter case prevails in thick-hBN samples, giving rise to extremely flat current-saturation plateaus (see Fig.SI4-f). Conversely, the small $V_S/V_g \simeq 0.5$ ratio in thin-hBN samples (AuS2-data in Fig.3-c), characterized by smeared saturation plateaus (see Fig.SI4-(d,e)), allows one to investigate conductance over an extended bias range $V/V_S \lesssim 4$.

We conclude our experimental report by analyzing the extended Schwinger-conductance regime in the low-bias AuS2-data which are plotted in Fig.3-d. The accessible experimental range of Schwinger conductance ($G_S \lesssim 0.6$ mS) exceeds the validity domain ($G_S \lesssim 0.2$ mS) of the low bias approximation (4), unveiling the sub-linearities involved in Eq.(3) (solid lines). Experimental data are in excellent agreement with the full Schwinger prediction, significantly deviating from the low bias approximation (dotted black line), and strongly deviating from the truncated-rate Schwinger conductance G_S^* (dash-dotted lines). This observation constitutes additional evidence of the relevance of the Schwinger theory [3].

The demonstration of the Schwinger effect in an effective field theoretical 1+1 dimensional system is the first of its kind and a confirmation of a crucial prediction of quantum electrodynamic field theory. It fulfills the promise of using graphene to emulate quantum electrodynamics [23], specifically here in its strong field sector. The use of condensed matter

analogs has already proven fruitful in cosmology [24], in particular with the observation of vortex formation in neutron-irradiated superfluid He-3 as an analogue of cosmological defect formation [25], or that of the analogue of black hole Hawking radiation [26].

Our experiment shows the capacity of Klein collimation to generate large local electric fields (peak effect). This opens a way for the exploration of Schwinger effect in different systems, like the massive Dirac fermions in bilayer graphene [27], or the massless fermions in 3d Weyl or Dirac semi-metals [28]. In this respect, theoretical challenges remain concerning the modeling of strongly out-of-equilibrium collimation and the emergence of the Schwinger gap. Our experiment also shows that prominent current saturations, with large saturation velocities, can be obtained in gapless graphene. Besides, the understanding of the Klein-Schwinger mechanism turns out to be the key for the optimization of large voltage-gain $A = \partial V/\partial V_g = G_m/G$ (see transconductance G_m in Fig.SI-II) in high-mobility graphene transistors, which is tunable from the $A \sim 10$ of thin-hBN AuS2 to the $A \sim 100$ of thick-hBN AuS3 according to the V_S/V_g ratio (see Table.SI-1).

Finally one may attempt to go deeper in the condensed matter analogy of QED, by investigating other manifestations of Schwinger effect like the full counting statistics of pair emission, or the vacuum polarization [3] which is a precursor of pair creation. This raises the question of the creation dynamics of Schwinger-pairs, which is an open field that can be investigated by dynamical transport and electromagnetic radiation spectroscopy.

III. AUTHORS CONTRIBUTIONS

AS, EBa and BP conceived the experiment. AS conducted device fabrication and measurements, under the guidance of DM and MR in the early developments. TT and KW have provided the hBN crystals. PV, JC, MOG, EBa, JT and BP developed the models and theoretical interpretations. AS, DM, CV, JMB, EBo, GF, CV, EBa and BP participated to the data analysis. AS, EBa, and BP wrote the manuscript with contributions from the coauthors.

IV. ACKNOWLEDGMENTS

The research leading to these results has received partial funding from the the European Union Horizon 2020 research and innovation program under grant agreement No.881603 Graphene Core 3.

V. ADDITIONAL INFORMATION

Competing financial interests: The authors declare no competing financial interests.

VI. DATA AVAILABILITY

Experimental data are open and available at DOI 10.5281/zenodo.7104630

VII. METHODS

Fabrication of ballistic graphene transistors. The hexagonal boron nitride encapsulated graphene heterostructures are fabricated with the standard pick-up and stamping technique, using a polydimethylsiloxane(PDMS)/ polypropylenecarbonate (PPC) stamp [29]. The gate is first fabricated on a high-resistivity Si substrate covered by 285nm SiO_2. Gate electrode is either a thin exfoliated graphite flake (thickness $\lesssim 15nm$) or a pre-patterned gold pad (thickness $70nm$) designed by laser lithography and Cr/Au metallisation. Deposition of the heterostructure on the backgate is followed by acetone cleaning of the stamp residues, Raman spatial mapping and AFM characterization of the stack. Graphene edge contacts are then defined by means of laser lithography and reactive ion etching, securing low contact resistance $\lesssim 1$ k$\Omega\mu$m. Finally, metallic contacts to the graphene channel are designed with a Cr/Au Joule evaporation, that also embeds the transistor in a coplanar waveguide geometry suited for cryogenic probe station microwave and noise characterization. The large transistor dimensions $L, W \gtrsim 10\mu$m secure moderate channel electric field $E \sim V/L \lesssim 10^6$V/m up to the MOSFET pinch-off at $V = V_g$, while their high mobility $\mu \gtrsim 6\text{m}^2\text{V}^{-1}\text{s}^{-1}$ at room temperature, and $\mu \gtrsim 35\text{m}^2\text{V}^{-1}\text{s}^{-1}$ at 10K, secures ballistic transport in the channel.

RF transport and noise measurement. Characterization of the ballistic graphene transistors is performed in a cryogenic probe station adapted to RF measurements up to 67GHz.

The DC measurements are performed using a Keithley 2612 voltage source to apply gate and bias. Noise measurements are enabled by the use of a Tektronix DPO71604C ultrafast oscilloscope for measurements up to 16GHz. The high-frequency signal coming from the device is amplified by a CITCRYO1-12D Caltech low noise amplifier in the $1-10$ GHz band, whose noise and gain have been calibrated against the thermal noise of a 50Ω calibration resistance measured at various temperatures between 10K and 300K in the probe station. For low frequency noise measurements in the $0.1-1$ MHz band, a NF-Corporation amplifier (SA-220F5) is used.

---

* Electronic address: aurelien.schmitt@phys.ens.fr

† Electronic address: emmanuel.baudin@phys.ens.fr

‡ Electronic address: bernard.placais@phys.ens.fr

[1] F. Sauter, *Z. Phys.* **69**, 742 (1931). *Uber das Verhalten eines Elektrons im homogenen elektrischen Feld nach der relativistischen Theorie Diracs*

[2] W. Heisenberg, H. Euler, *Z. Phys.* **98**, 714 (1936). *Consequences of Dirac's theory of positrons*

[3] J. S. Schwinger, Phys. Rev. **82**, 664 (1951). *On gauge invariance and vacuum polarization*

[4] C. Itzykson and J. B. Zuber, *Quantum Field Theory*, McGraw-Hill (2006).

[5] R. Schutzhold, H. Gies, G. Dunne, *Phys. Rev. Lett* **101**, 130404 (2008). *Dynamically assisted Schwinger mechanism*

[6] S.P. Gavrilov. and D.M. Gitman, *Phys. Rev. D* **53**, 7162 (1996). *Vacuum instability in external fields*

[7] R. Schutzhold, *Adv. Sci. Lett* **2**, 121 (2009). *Recreating Fundamental Effects in the Laboratory?*

[8] A. Shytov, M. Rudnerb, N. Guc, M. Katsnelson, L. Levitov, *Solid State Communications* **149**, 10987 (2009). *Atomic collapse, Lorentz boosts, Klein scattering, and other quantum-relativistic phenomena in graphene*

[9] B. Dora, R. Moessner, *Phys. Rev. B* **81**, 165431 (2010). *Non-linear electric transport in graphene: quantum quench dynamics and the Schwinger mechanism*

[10] S. P. Gavrilov, D. M. Gitman, N. Yokomizo, *Phys. Rev. D* **86**, 125022 (2012). *Dirac fermions in strong electric field and quantum transport in graphene*

[11] M. I. Katsnelson, G. E. Volovik, *JETP Letters* **95**, 411 (2012). *Quantum electrodynamics*

with anisotropic scaling: Heisenberg-Euler action and Schwinger pair production in the bilayer graphene

[12] N. Vandecasteele, A. Barreiro, M. Lazzeri, A. Bachtold, F. Mauri, *Phys. Rev. B.* **82**, 045416 (2010). *Current-voltage characteristics of graphene devices: Interplay between Zener-Klein tunneling and defects.*

[13] A. I. Berdyugin, N. Xin, H. Gao, S. Slizovskiy, Z. Dong, S. Bhattacharjee, P. Kumaravadivel, S. Xu, L. A. Ponomarenko, M. Holwill, D. A. Bandurin, M. Kim, Y. Cao, M. T. Greenaway, K. S. Novoselov, I. V. Grigorieva, K.Watanabe, T. Taniguchi, V. I. Falko, L. S. Levitov, R. K. Kumar, A. K.Geim, *Science* **375**, 430 (2022). *Out-of-equilibrium criticalities in graphene superlattices*

[14] W. Yang, S. Berthou, X. Lu, Q. Wilmart, A. Denis, M. Rosticher, T. Taniguchi, K. Watanabe, G. Fève, J.M. Berroir, G. Zhang, C. Voisin, E. Baudin, B. Plaçais, *Nature Nanotechnol.* **13**, 47 (2018). *A graphene Zener-Klein transistor cooled by a hyperbolic substrate*

[15] E. Baudin, C. Voisin, B. Plaçais, *Adv. Funct. Materials* **30**, 1904783 (2020). *Hyperbolic Phonon Polariton Electroluminescence as an Electronic Cooling Pathway*

[16] I. Meric, M. Y. Han, A. F. Young, B. Ozyilmaz, P. Kim, K. L. Shepard, *Nature Nanotech.* **3**, 654-659, (2008). *Current saturation in zero-bandgap, top-gated graphene field-effect transistors*

[17] Q. Wilmart, M. Boukhicha, H. Graef, D. Mele, J. Palomo, M. Rosticher, T. Taniguchi, K. Watanabe, V. Bouchiat, E. Baudin, J-M. Berroir, E. Bocquillon, G. Fève, E. Pallecchi, B. Plaçais, *Appl. Sci.* **10**, 446, (2020). *High-Frequency Limits of Graphene Field-Effect Transistors with Velocity Saturation*

[18] A. Pierret, D. Mele, H. Graef, J. Palomo, T. Taniguchi, K. Watanabe, Y. Li, B. Toury, C. Journet, P. Steyer, V. Garnier, A. Loiseau, J-M. Berroir, E. Bocquillon, G. Fève, C. Voisin, E. Baudin, M. Rosticher, B. Plaçais, *Mater. Res. Express* **9**, 065901 (2022). *Dielectric permittivity, conductivity and breakdown field of hexagonal boron nitride*

[19] S.M. Sze and K. Ng, *Physics of Semiconductor Devices, Wiley-2007-3rd edition*, Chap 7, p.389.

[20] V. V. Cheianov, V. I. Falko, *Phys. Rev. B* **74**, 041403(R) (2006) *Selective transmission of Dirac electrons and ballistic magnetoresistance of n-p junctions in graphene*

[21] J. Cayssol, B. Huard, D. Goldhaber-Gordon, *Phys. Rev. B* **79**, 075428 (2009). *Contact resistance and shot noise in graphene transistors.*

[22] R. Danneau, F. Wu, M. F. Craciun, S. Russo, M. Y. Tomi, J. Salmilehto, A. F. Morpurgo, P. J. Hakonen, *Phys. Rev. Lett.* **100**, 196802 (2008). *Shot Noise in Ballistic Graphene*

[23] K.S. Novoselov, *Rev. Mod. Phys.* **83**, 837 (2011) *Nobel lecture: Graphene: Materials in the flatland*

[24] W.H. Zurek, *Physics Reports* **276**, 177 (1996). *Cosmological experiments in condensed matter systems*

[25] V.M. Ruutu, V.B. Eltsov, A. Gill, T.W. Kibble, M. Krusius, Yu. G. Makhlin, B. Plaçais, G.E. Volovik, Wen Xu, *Nature* **382**, 334 (1996). *Vortex formation in neutron-irradiated superfluid 3He as an analogue of cosmological defect formation*

[26] J.R.M. de Nova, K. Golubkov, K.V.I. Kolobov, J. Steinhauer, *Nature* **569**, 688 (2019) *Observation of thermal Hawking radiation and its temperature in an analogue black hole*

[27] M. I. Katsnelson, G. E. Volovik, *JETP Letters* **95**, 411 (2012). *Quantum electrodynamics with anisotropic scaling: Heisenberg-Euler action and Schwinger pair production in the bilayer graphene*

[28] M. I. Katsnelson, G. E. Volovik, *J. Low Temp. Phys.* **175**, 655 (2014). *Topological Matter: Graphene and Superfluid He*

[29] M. Yankowitz, Q. Ma, P. Jarillo-Herrero, B. J. LeRoy, *Nature Reviews Physics* **1**, 1125 (2019). *van der Waals heterostructures combining graphene and hexagonal boron nitride*

[30] ξ is the typical interaction radius per electron (for $n_s t_{hBN}^2 = 1$) fitting in a junction length $\Lambda \sim t_{hBN}$.

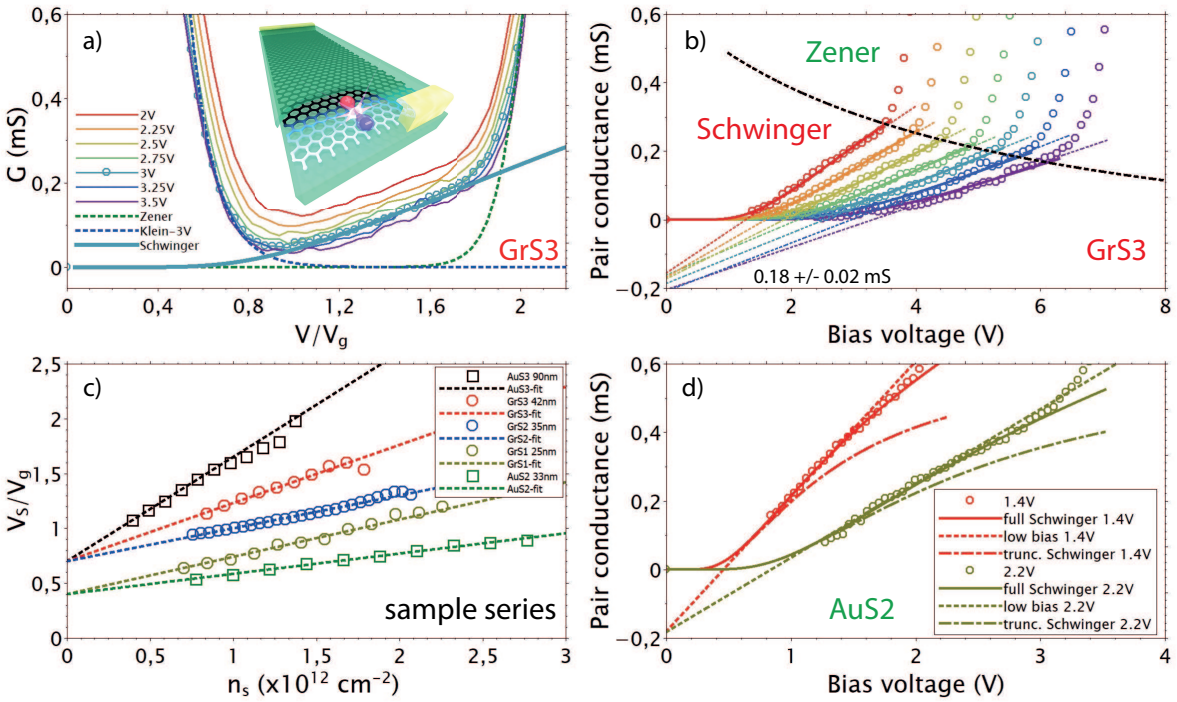

FIG. 3: Klein-Schwinger effect in long ballistic transistors. Panel-a: blow-up of GrS3 conductance in Fig.2-b. The fully developed gap at large doping (dashed blue and green lines of the $V_g = 3$ V data), unveils the Schwinger-pair contribution (thick turquoise line) corresponding to $V_S \simeq 1.4V_g$. Inset: artist view of the Klein-Schwinger mechanism. At lower doping, where the Schwinger contribution is embedded in a finite Klein contribution, the pair contribution is extracted by a 3-parameters fit of conductance data according to the law $G(V) = G_S(V/V_S) + G(0)e^{-V/V_{sat}}$. Panel-b: the pair contribution $G(V) - G(0)e^{-V/V_{sat}}$ (same color code as in panel a), reveals the low-bias scaling of the Schwinger conductance (4) with $G_0 \simeq 0.18 \pm 0.02$ mS and $V_S = 0.7V_g + 0.15V_g^2$. The Zener regime is signaled by a sharp increase of pair conductance above the Schwinger-Zener boundary (dotted black line) set by $G_S(V = V_Z = 1.9V_g)$. Panel-c: linear increase of the $V_S/V_g(n_s)$ ratio with doping observed in the full transistor series (see Supplementary Fig.SI-7) where Schwinger-pair conductance scaling is reported with consistent values of G_0. The slope increases with dielectric thickness (see main text). V_S/V_g is minimized in sample AuS2 ($L \times W \times t_{hBN} = 10.5 \times 15 \times 0.035$ μm) and maximized in sample AuS3 ($L \times W \times t_{hBN} = 11.1 \times 11.4 \times 0.090$ μm). Panel-d: broad range ($V/V_S \lesssim 4$) Schwinger conductance at low doping in AuS2 where $V_S/V_g \simeq 0.5$ showing the quantitative agreement with Eq.(3) (solid lines) that deviates from the low-bias Eq.(4) approximation (dotted lines), and from the truncated approximation G_S^* (dash-dotted lines).

Mesoscopic Klein-Schwinger effect in graphene

(Supplementary Information)

A. Schmitt,[1,*] P. Vallet,[2] D. Mele,[1,3] M. Rosticher,[1] T. Taniguchi,[4] K. Watanabe,[4] E. Bocquillon,[1,5] G. Fève,[1] J.M. Berroir,[1] C. Voisin,[1] J. Cayssol,[2] M. O. Goerbig,[6] J. Troost,[1] E. Baudin,[1,†] and B. Plaçais[1,‡]

[1]*Laboratoire de Physique de l'Ecole normale supérieure, ENS, Université PSL, CNRS, Sorbonne Université, Université de Paris, 24 rue Lhomond, 75005 Paris, France*

[2]*Laboratoire Ondes et Matière d'Aquitaine, 351 cours de la libération, 33405 Talence, France*

[3]*Univ. Lille, CNRS, Centrale Lille, Univ. Polytechnique Hauts-de-France, Junia-ISEN, UMR 8520-IEMN, F-59000 Lille, France.*

[4]*Advanced Materials Laboratory, National Institute for Materials Science, Tsukuba, Ibaraki 305-0047, Japan*

[5]*II. Physikalisches Institut, Universität zu Köln, Zülpicher Strasse 77, 50937 Köln*

[6]*Laboratoire de Physique des Solides, CNRS UMR 8502, Univ. Paris-Sud, Université Paris-Saclay, F-91405 Orsay Cedex, France*

(Dated: September 26, 2022)

I. SCHWINGER EFFECT IN VARIOUS DIMENSIONS

Quantum electrodynamics predicts a pair creation rate, per unit volume, area or length depending on dimensionality, as given by [1], with $E_S = \frac{m^2c^3}{e\hbar}$ the Schwinger field,

$$w_{3d} = \frac{(eE)^2}{4\pi^3 c\hbar^2}\sum_{n\geq 1}\frac{e^{-n\pi\frac{E_S}{E}}}{n^2} \quad , \quad w_{2d} = \frac{eE}{2\pi^2\hbar}\sqrt{\frac{eE}{c\hbar}}\sum_{n\geq 1}\frac{e^{-n\pi\frac{E_S}{E}}}{n^{3/2}} \quad , \quad w_{1d} = \frac{eE}{\pi\hbar}\sum_{n\geq 1}\frac{e^{-n\pi\frac{E_S}{E}}}{n} \quad . \tag{1}$$

When adapted to condensed matter, speed of light c is replaced by Fermi velocity v_F and the rest energy is substituted with the gap Δ_S. The pair partners being dissosicated in the strong electric field, one can thus write a mesoscopic pair current, with a mesoscopic Schwinger field $E_S = \frac{\Delta^2}{e\hbar v_F}$ and voltage $V_S = \frac{\Lambda\Delta_S^2}{e\hbar v_F}$, as

$$J_{3d} = \frac{e^2E^2\Lambda}{2\pi^3 v_F\hbar^2}\sum_{n\geq 1}\frac{e^{-n\pi\frac{E_S}{E}}}{n^2} \quad , \quad J_{2d} = \frac{2g_sg_ve^2}{\pi h}\sqrt{\frac{e\Lambda^2}{\hbar v_F}}E^{3/2}\sum_{n\geq 1}\frac{e^{-n\pi\frac{E_S}{E}}}{n^{3/2}} \tag{2}$$

$$I_{1d} = \frac{4g_sg_ve^2}{h}V_{ds}\sum_{n\geq 1}\frac{e^{-n\pi\frac{V_S}{V_{ds}}}}{n} \quad . \tag{3}$$

Not specific to Schwinger effect, the $J_{3d} \propto E^2 e^{-\frac{Cte}{E}}$ is reminiscent of field emission according to the Fowler-Nordheim mechanism, which is a non-relativistic variant, corresponding to quantum tunneling across a triangular barrier [2,3], with

$$J_{FN} = \frac{e^3 m_0 E^2}{16\pi^2 m^*\hbar\phi}e^{-\pi\frac{E_{FN}}{E}} \qquad E_{FN} = \frac{4\sqrt{2m^*\phi^3}}{3\pi e\hbar} \sim \frac{4\sqrt{2}}{3\pi}\frac{\phi^2}{e\hbar v_F} \quad , \tag{4}$$

where m_0 and m^* are the bare and effective electron masses, ϕ is the barrier height. It differs from Eq.(2) in the non-universal character of the pre-factor and critical field.

Mesoscopic Schwinger effect has been considered to describe non-linear transport in gapless neutral 2d-graphene [4–8], with :

$$E_S = 0 \qquad J_{2d} = 2.612\frac{2g_sg_ve^2}{\pi h}\sqrt{\frac{e\Lambda^2}{\hbar v_F}}E^{3/2} \quad , \tag{5}$$

where Λ is the length of the charge neutrality region, and $g_s = g_v = 2$ are the spin and valley degeneracy of graphene. The non-linear Schwinger-pair contribution exceeds the single particle tunneling conductivity $\sigma_{2d} = \frac{g_sg_ve^2}{\pi h}$ [9,10] above a bias voltage $V_{2d} \sim \hbar v_F/e\Lambda \sim 1\text{mV}$ (for $\Lambda = 1\mu\text{m}$).

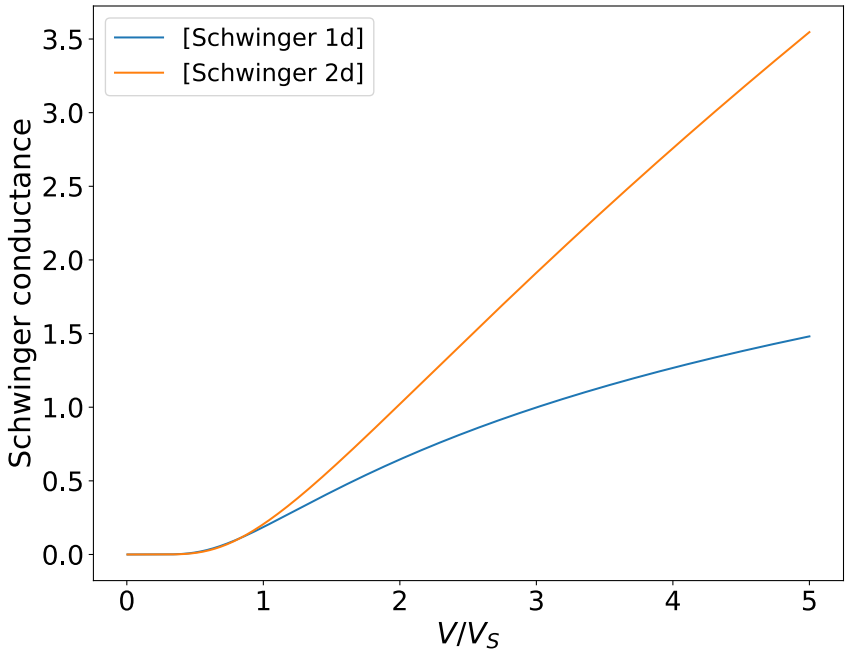

FIG. SI-1: Representation of the functional forms (terms in brackets) of equations (6) and (7) for 1d and 2d massive Schwinger effect. The two forms have the same threshold and low-bias development but differ at large bias. The 2d conductance is not universal and depends on the ratio of the sample width W to the Compton length Λ_C which is typically a large number. It is larger but also linear over a wider bias range than the 2d-Schwinger conductance.

The 2d massive Schwinger effect differs from the 1d massive Schwinger effect studied in the main text. The 1d and 2d conductance read :

$$G_{1d} = 4 \left(\frac{g_s g_v e^2}{h}\right) \times \left[\pi\sqrt{\frac{V}{V_S}}\,\frac{1}{e^{\pi V_S/V}-1} + \ln\left(\frac{1}{1-e^{-\pi V_S/V}}\right)\right] \tag{6}$$

$$G_{2d} = \frac{2W}{\pi\Lambda_C}\left(\frac{g_s g_v e^2}{h}\right) \times \left[\frac{3}{2}\sqrt{\frac{V}{V_S}}\sum_{n\geq 1}\frac{e^{-n\pi V_S/V}}{n^{3/2}} + \pi\sqrt{\frac{V_S}{V}}\sum_{n\geq 1}\frac{e^{-n\pi V_S/V}}{n^{1/2}}\right] \quad , \tag{7}$$

where W is the sample width and $\Lambda_C = \sqrt{\frac{v_F\hbar}{eE_S}} \lesssim 10$nm the Compton length. Compared to the 1d Schwinger conductance, the 2d-conductance prefactor is not universal and much larger by a factor $W/\Lambda_C(V_g) \sim 1000$. Evidence of the universal character of the measured conductance in the ballistic transistors is given in Figure SI-7 and Figure 3-b from the main text, that all show the same universal zero-bias extrapolate $G = -0.18 \pm 0.02$ despite contrasted values of W and E_S. Apart from the prefactor, the two formulae also show different behavior with respect to bias voltage, as shown in Figure SI-1. The sublinear

dependence of the 1d-conductance of Eq.(6) is clearly seen in Fig. SI-7d) and e), and in Figure 3-d from the main text.

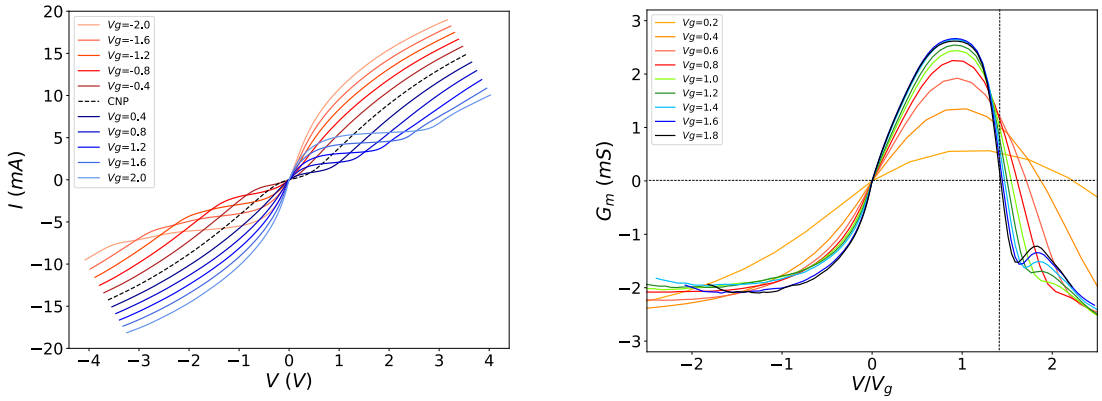

FIG. SI-2: Overview of ballistic pinch-off in hBN-encapsulated graphene transistor GrS1, of dimensions $L \times W \times t_{hBN} = 13 \times 17 \times 0.025$ μm, mobility $\mu = 6.3$ m^{2}V^{-1}s^{-1}, and contact resistance $R_c = 80$ Ω. Left: full bipolar representation. Pinch-off free transport is observed in the drain carrier accumulation regime for Sign$(V \times V_g) < 0$. It shows standard intra-band velocity saturation by optical phonons (OP), followed by the Zener regime.. Pinch-off is observed under drain depletion, for a channel voltage $V = V_{bias} - R_c I \sim V_g$, with broad ($V \sim 0.3$–$1.5V_g$) current plateaus. Pinch-off current is depleted by a factor two below the drain-accumulation counterpart, falling below the massless charge neutrality Zener level (CNP, black dotted line). Pinch-off plateaus terminate as an instability toward the ohmic Zener regime, which is rejected here above $V_Z \gtrsim 1.5V_g$ by Pauli blocking. Right: DC transconductance scaling as function of V/V_g, concentrating on positive V_g values. It underlines the asymmetry between positive and negative V regimes, with a negative transconductance for negative V, illustrating the increase of current with increasing doping. For positive V, the transconductance turns strongly negative, highlighting the depletion of the pinch-off current below the zero-doping CNP value. The transconductance changes sign slightly above pinch-off at $V \simeq 1.4V_g$, corresponding to a current $I \simeq 1.1I_{sat}$.

II. OVERVIEW OF BALLISTIC PINCH-OFF IN SAMPLE GRS1

A complete panorama of ballistic pinch-off in graphene transistors can be found in sample GrS1, of dimensions $L \times W \times t_{hBN} = 13 \times 17 \times 0.025$ μm, shown in Fig.SI-2. Thanks

to fortuitous equal electron and hole mobilities ($\mu = 6.3\ m^2V^{-1}s^{-1}$), the current-voltage characteristics in Fig.SI-2-a are fully symmetric. We can distinguish between two different regimes. When Sign$(V \times V_g) < 0$, increasing V causes an accumulation of charge carriers on the drain side, but the channel stays unipolar. In this case we observe pinch-off-free transport, which shows standard intra-band velocity saturation by optical phonons followed by the Zener inter-band regime with a doping-independent conductance $G_Z(V) \sim 2.5$mS [11]. When Sign$(V \times V_g) > 0$, pinch-off is observed under drain depletion for a voltage $V \sim V_g$, with broad current saturation plateaus ($V \sim 0.3$–$1.5V_g$). These plateaus terminate as an instability towards the ohmic Zener regime, where charge transport becomes bipolar in the channel. Due to the carrier depletion at the drain, the pinch-off current is depleted below the massless charge neutrality Zener level, suggesting the existence of a doping-induced conductance gap.

The two different transport regimes can also be identified in the transconductance G_m in Fig.SI-2-b. For sake of visibility, we focus here on the $V_g > 0$ curves. The drain carrier accumulation for $V < 0$ is associated with a negative transconductance, as higher gate values, corresponding to higher doping, lead to higher current. On the other hand, the negative values of G_m for positive bias confirm the pinch-off depletion of the current.

Suitable for the study of Klein-collimation, the sample GrS1 suffers from a relatively low electronic mobility and a low dielectric thickness t_{hBN}, which results in a early onset of the Zener conductance and a reduced accessible voltage range. The hBN thickness indeed determines the range of accessible bias and gate voltages that can be applied on the device without generating strong leak currents and finally the breakdown of the insulator [12] ; the leakage can be due to a high gate voltage, but can also appear below the drain electrode if the voltage difference $V - V_g$ becomes too important. As a consequence, the raw differential conductance shows no signature of Schwinger effect.

However, the subtraction of the fitted Klein conductance allows restoring the visibility of the 1d-Schwinger conductance below the Zener onset voltage, as shown in Figure SI-7-a. Further study of this device can be found in Section IV.

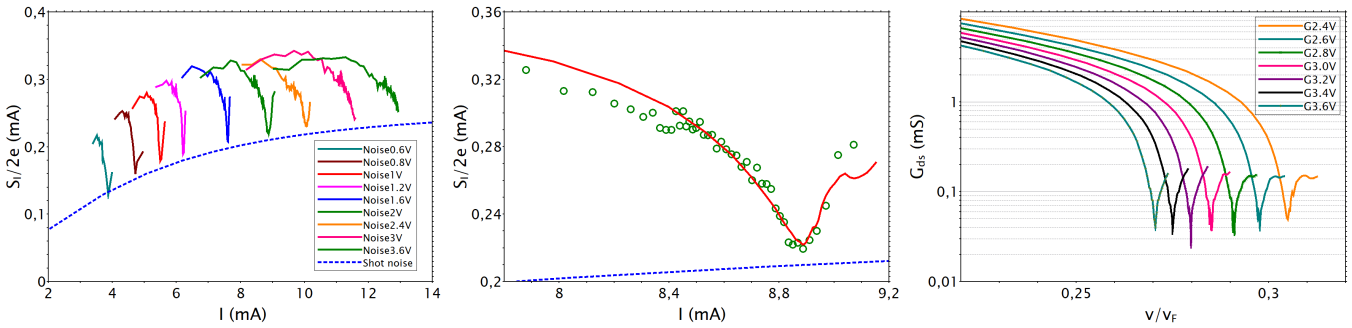

FIG. SI-3: Current noise signature of Klein-collimation pinch-off in sample GRS2. Dimensions are $L\times W\times t_{hBN} = 10.5\times15\times0.035$ μm. Left: high-frequency white noise $S_I(I)$, measured at $T_0 = 10$ K in the 1–10 GHz band using Caltech Low Noise Amplifiers (model CITCRYO1-12D). It shows a sharp dip at pinch-off mapping the conductance dip (right panel). Note that the noise dip occurs at a current 10 percent larger than the conductance dip, due to the transconductance correction to the Johnson-Nyquist formula for a transistor $S_{therm} \simeq 4(G+\beta G_m)k_BT_e$. Considering that noise is the sum of a thermal contribution, $S_{th} = 4Gk_BT_e$, and a shot-noise contribution, $S_{shot} = 2eI\mathcal{F}$ where $\mathcal{F} \lesssim 1$ is a Fano factor, we extract the pinch-off shot noise $S_{shot}/2e(I_{sat}) \simeq I_0 \times I_{sat}/\sqrt{I_1^2 + I_{sat}^2}$ (dashed blue line), with $I_0 = 0.26$ mA and $I_1 = 6$ mA. This translates into a tiny pinch-off current Fano factor, $\mathcal{F} = I_{shot}/I_{sat} \simeq I_0/\sqrt{I_{sat}^2 + I_1^2} \lesssim 0.04$, that vanishes for $I_{sat} \gg I_1$. Center: Zoom on the high-frequency white noise $S_I(I)$ close to pinch-off for $V_g = 2V$. Using the measured $G(I)$, we fit noise data (dashed red line) to estimate the electronic temperature on the current saturation plateau ($I \simeq I_{sat}$) at $T_e \sim 1100\text{K} \times V/V_g$ ($V_g = 2$ V), which corresponds to $k_BT_e/eV_g \simeq 0.1$. Right: Conductance-velocity $G(v/v_F)$ representation of ballistic pinch-off at $T_0 = 10$ K. The velocity is defined as the velocity at the source electrode by $v = \frac{I}{C_gV_gW}$.In this representation, the broad $V \simeq 1$–$2V_g$ conductance gap collapses into a singular point at $G(I_{sat}) \lesssim 0.1$ mS.

III. NOISE CHARACTERIZATION OF KLEIN COLLIMATION

Additional signatures of ballistic pinch-off can be found in the current noise S_I, which is measured in sample $GrS2$. It is representative of the series and actually quite similar to sample $GrS3$ of the main text. We distinguish different noise contributions according to frequency: the low-frequency flicker noise, which is measured at sub-MHz frequency and is described in the main text, and the flicker-free white thermal/shot noise, which is measured at GHz frequency.

The GHz noise (measured at $T = 10$ K) is plotted in Fig.SI-3-a as function of current. It exhibits a sharp dip at current saturation ($I \gtrsim I_{sat}$) which is reminiscent of the conductance dip observed in the $G(v/v_F)$ data of Fig.SI-3-c. We thus analyze the $S_I(I)$ dependence as the sum of two terms: a thermal contribution $S_{therm} \simeq 4G_{ds}k_BT_e$, where T_e is the hot-electron temperature, and a shot-noise contribution $S_{shot} = 2eI\mathcal{F}$, where $\mathcal{F} \lesssim 1$ is a Fano factor. In this interpretation, the GHz noise dip corresponds to the vanishing of $S_{therm}(I_{sat}) \propto G(I_{sat}) \to 0$ at current saturation, leaving shot noise as the residual noise. This assumption is supported by the $S_I(I) - S_I(I_{sat}) \propto S_{therm}(I)$ dependence which can be fitted in the current saturation regime assuming a $T_e(I) = T_e(I_{sat})V/V_g$ proportional to Joule power $P \simeq I_{sat}V$ (red dotted line in Fig.SI-3-b with $T_e \sim 1100$K for $V_g = 2$ V). Actually, the thermal noise of a transistor, $S_{therm} \simeq 4(G+\beta G_m)k_BT_e$ deviates from the standard Johnson-Nyquist formula for a two terminal resistor by an additive correction proportional to the transconductance G_m. This effect has been demonstrated in carbon nanotube transistors in Ref.[13]. The abrupt sign change of G_m observed at $V/V_g \simeq 1.4$ in Fig.SI-2-b, actually secures a full compensation of the residual conductance which explains the full suppression of thermal noise observed at $I/I_{sat} \simeq 1.1$ in Fig. SI-3-a.

Assigning the $S_I(I_{ds})$ minima to shot noise we deduce a pinch-off shot noise $S_{shot}(I_{sat}) \simeq 2eI_0 \times I_{sat}/\sqrt{I_1^2 + I_{sat}^2}$ (dashed blue line), with $I_0 = 0.26$ mA and $I_1 = 6$ mA. It translates into a tiny Fano factor, $\mathcal{F} = I_{shot}/I_{sat} \simeq I_0/\sqrt{I_{sat}^2 + I_1^2} \lesssim 0.04$, that vanishes for $I_{sat} \gg I_1$. We regard the presence of shot noise as a proof of the existence of a pinch-off junction, and attribute its tiny Fano factor to a consequence of strong collimation effect.

IV. KLEIN-SCHWINGER EFFECT IN THE FULL DEVICE SERIES

Besides the sample GrS3 extensively described in the main text, five other samples have been measured and characterized. All of them show consistent Klein-Schwinger effect, albeit with a somewhat lower visibility due to non-optimal geometrical properties or electronic mobility. Yet, the subtraction of the fitted Klein conductance, following the same procedure as in the main text, allows restoring a larger visibility of the 1d-Schwinger conductance for all the devices. A summary of the properties of the five devices can be found in Table SI-1. For completeness we have reproduced the data of sample GrS3 analyzed in main text.

The current-voltage curves of the six devices series are shown in Figure SI-4. We always

Sample	**L** μm	**W** μm	t_{hBN} nm	t_{Graph} nm	μ $\frac{m^2}{Vs}$	R_c Ω	A -	σ_Z mS	$\frac{V_Z}{V_g}$ -	$\frac{eV_{sat}}{\mu_s}$ -	$\frac{V_S}{V_g}$ -	G_0 mS
GrS1	13	17	25	15	6.3	80	50	2.5	1.25	2.6	$0.4 + 0.37\ n_s$	0.17 ± 0.02
GrS2	10.5	15	35	7	13	80	40	1	1.7	3.3	$0.7 + 0.30\ n_s$	0.18 ± 0.01
GrS3	15	10	42	7	12	120	70	1	1.9	2.8	$0.7 + 0.53\ n_s$	0.18 ± 0.02
AuS1	10	13.4	34	/	8	80	7	1.5	1.7	3.7	$0.4 + 0.17\ n_s$	0.18 ± 0.02
AuS2	16	10.6	32	/	13	80	11	1	1.5	4.9	$0.4 + 0.18\ n_s$	0.18 ± 0.01
AuS3	11.1	11.4	90	/	11	95	100	0.7	1.6	/	$0.7 + 1.05\ n_s$	0.17 ± 0.04

TABLE SI-1: Summary of the properties of the device series studied in the main text (GrS3) and in the supplementary (GrS1 and GrS2, AuS1, AuS2, AuS3). Base parameters presented in the first columns include the geometrical properties L, W, t_{hBN}, t_{Graph} for the devices on graphite gate, mobility and contact resistance. Also displayed is the maximum value of the voltage gain $A = \frac{\partial V}{\partial V_g}$. The next 4 columns correspond to the parameters that are responsible for the unveiling and visibility of the Klein-Schwinger effect in the different devices : V_Z is the Zener onset voltage, where a Zener conductance σ_Z activates. It has to be (notably) higher than the Schwinger voltage V_S that triggers the Schwinger conductance, and whose doping dependence is shown in the next-to-last column. The doping-dependent saturation voltage V_{sat}, extracted from the dependence $G = G(0)Exp\left[-\frac{V}{V_{sat}}\right]$ in the Klein regime, is a metrics of the Klein collimation and defines the beginning of the conductance gap, later terminated by Zener regime. The last column G_0 corresponds to the zero-bias extrapolate of the Schwinger pair conductance.

subtract in the bias voltage the voltage drop $R_C I$ across the contact resistance. All the devices exhibit broad current saturation plateaus, with, however, an incomplete saturation (differential resistance peak $G^{-1} \lesssim 5k\Omega$) for devices AuS1 (panel d) and Au-S2 (panel e). The current saturation plateaus are terminated by the onset of Zener conductance at a Zener field $V_Z = 1.25 - 2V_g$ depending on the device. Detailed values can be found in Table SI-1.

All of the 6 devices exhibit consistent Klein collimation, as is described by the semi-log representation of the differential conductance scaling $G(V/V_g)$ in Figure SI-5. It shows an exponential decay of the Klein conductance for all samples, with a sample-dependent slope that tunes the depth of the conductance gap. For instance, sample AuS3 (panel f)

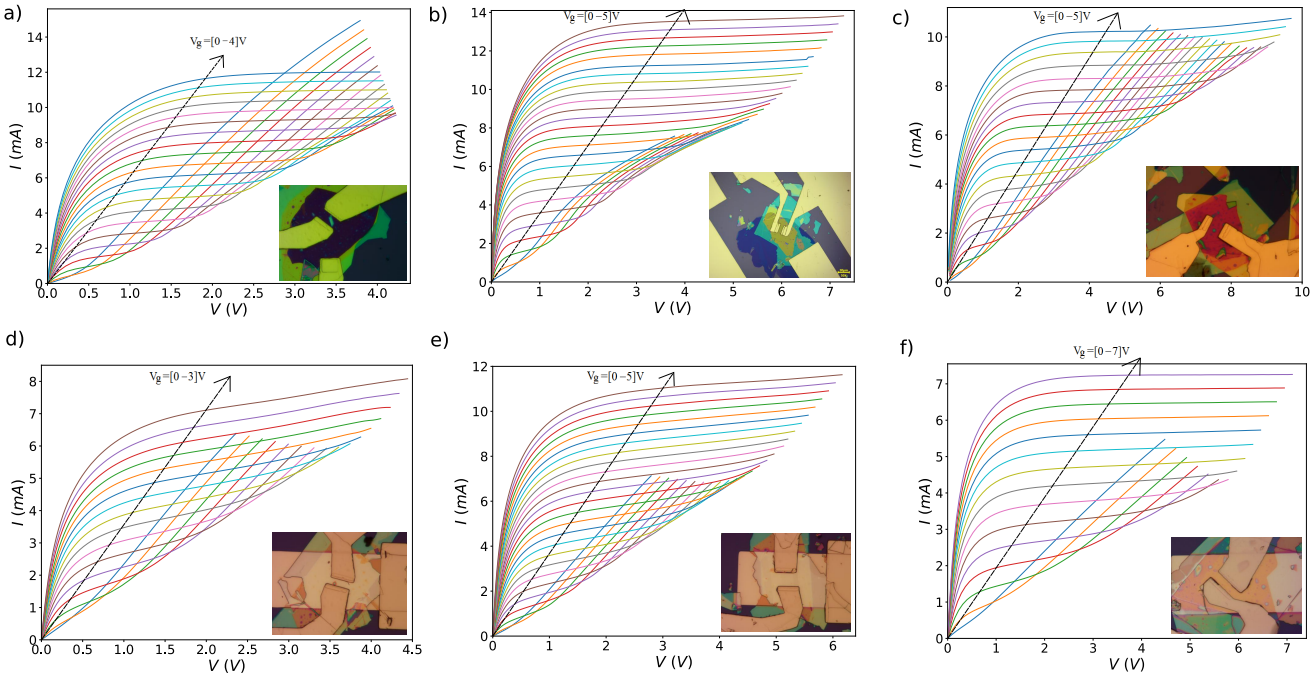

FIG. SI-4: Current-voltage curves of the device series GrS1 (panel a), GrS2 (panel b), GrS3 (panel c), AuS1 (panel d), AuS2 (panel e) and AuS3 (panel f). Inset of each panel shows an optical image of the device. Actual device dimensions are collected in Table SI-1. The properties of the device series are summarized in Table SI-1. The applied gate voltages correspond to a charge carrier density at the source ranging from 0 to $1.5 - 2.5\ 10^{12}\,\mathrm{cm}^{-2}$ depending on the device.

exhibits a steep conductance decay by three orders of magnitude at pinch-off, with differential conductance dropping below $10\mu S$, whereas the conductance gap is very shallow in samples AuS1 (panel d) and AuS2 (panel e). The doping-dependent saturation voltage V_{sat}, plotted in inset in the different panels, presents consistently a linear relation with the doping $eV_{sat} = \alpha\mu_S$ with $\alpha \sim 3$ in the different samples (except for AuS3 where $V_{sat} = Cte$, see Table SI-1).

In order to study 1d-Schwinger pair conductance in the full series, Figure SI-6 shows a zoom of the differential conductance as function of V/V_g in the conductance gap region, where Schwinger conductance appears on top of current saturation. The visibility of Schwinger effect differs on the different devices, yet the 3-parameters KSE fits closely match the data on all of them (dotted lines in the figure). Sample GrS1 (panel a) demonstrates a very narrow conductance gap due to early Zener onset at V_Z $1.25V_g$, hiding Schwinger conductance. Samples GrS2 and GrS3 (panel b and c) are very similar and both exhibit a wide conductance gap due to a complete current saturation and a rejection of the Zener voltage above $1.7V_g$.

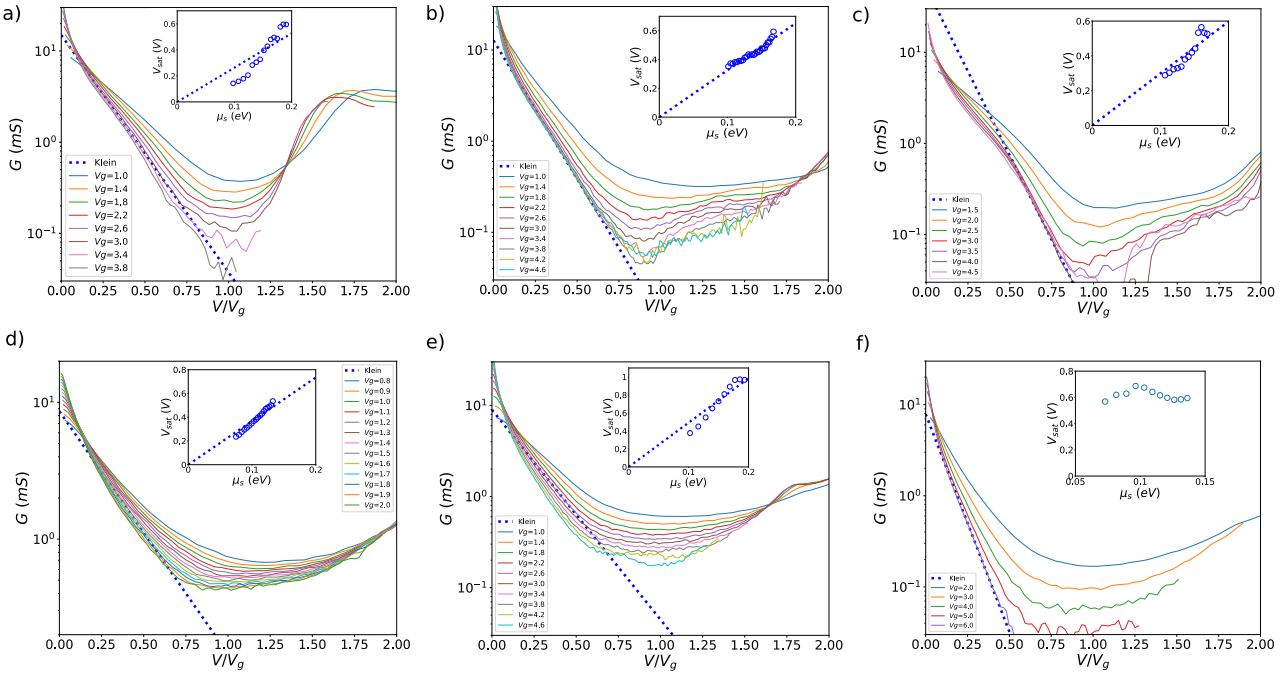

FIG. SI-5: Semi-log representation of the differential conductance scaling $G(V/V_g)$, showing the exponential decay of the saturation dependence $G = G(0)exp(-\frac{V}{V_{sat}})$ (dotted blue line) for the device series GrS1 (panel a), GrS2 (panel b), GrS3 (panel c), AuS1 (panel d), AuS2 (panel e) and AuS3 (panel f). Inset of each panel shows the evolution of the saturation voltage V_{sat} as function of the doping, with a linear relation for all devices except AuS3. Numerical values can be found in Table SI-1.

Due to the Klein conductance $G_K \propto W$ and the Zener threshold set by Pauli blocking $V_Z \propto L$, sample GrS2 exhibits a narrower conductance gap compared to GrS3. 1d-Schwinger conductance is still clearly visible in the conductance gap.

The devices on Au gates have a lower visibility for the Schwinger conductance here. Sample AuS1 (panel d) and AuS2 (panel e), whose properties are very similar (see Table SI-1), demonstrate a very shallow conductance gap $G_{min} \sim 0.2 - 0.4mS$, making it uneasy to see a direct signature of Schwinger regime via its onset. Sample AuS3 (panel f), with its thicker dielectric $t_{hBN} = 90nm$, exhibits an extremely deep and large conductance gap. However, the large dielectric thickness also shifts the Schwinger voltage towards higher values $V_S \gtrsim 1.5V_g$, setting the onset of the Schwinger conductance near the Zener onset and therefore reducing its visibility.

The KSE fits performed on the 6 devices give the values of the Schwinger voltage V_S, which

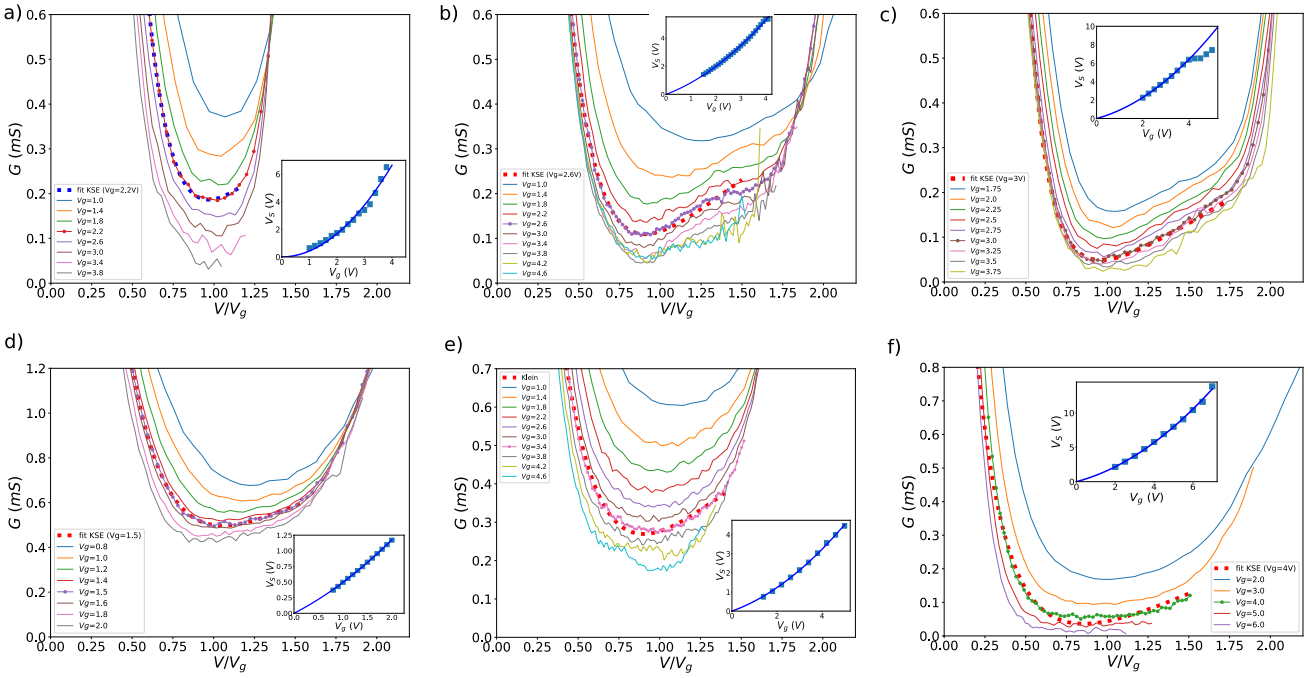

FIG. SI-6: Klein-Schwinger effect in the sample series GrS1 (panel a), GrS2 (panel b), GrS3 (panel c), AuS1 (panel d), AuS2 (panel e) and AuS3 (panel f). The red dotted lines on each figure show an example of a three-parameter fit $G = G_S(V_S) + G(0)e^{-V/V_{sat}}$ performed in the $V_{sat} \lesssim V \lesssim V_Z$ range ; due to different geometrical and electronic properties, the Schwinger visibility is variable on the different devices. Inset in each panel shows the super-linear dependence of the Schwinger voltage as function of gate voltage $\frac{V_S}{V_g} = a + bn_s$ deduced from the fits. The values of the coefficients a and b can be found in Table SI-1 for each device.

is plotted in the insets as function of the gate voltage V_g. For analysis of these data, we refer to Figure 3-c in the main text.

The visibility of the 1d-Schwinger pair conductance is determined by the combined vanishing of Klein intraband conductance and Zener interband conductance. Using the KSE fits, performed in Klein and Schwinger regimes, to subtract the fitted contribution of Klein conductance allows revealing the Schwinger conductance on a broader range of bias, a procedure which has been described in the main text (see Figure 3-b). The resulting pair conductance is plotted for all devices in Figure SI-7, revealing ubiquitous 1d-Schwinger conductance for the sample series. Agreement with the theoretical formula (solid lines) is excellent, up to a a Zener voltage corresponding to a steep increase of pair conductance.

Whereas the 1d-Schwinger conductance was already clearly visible in samples GrS2 and

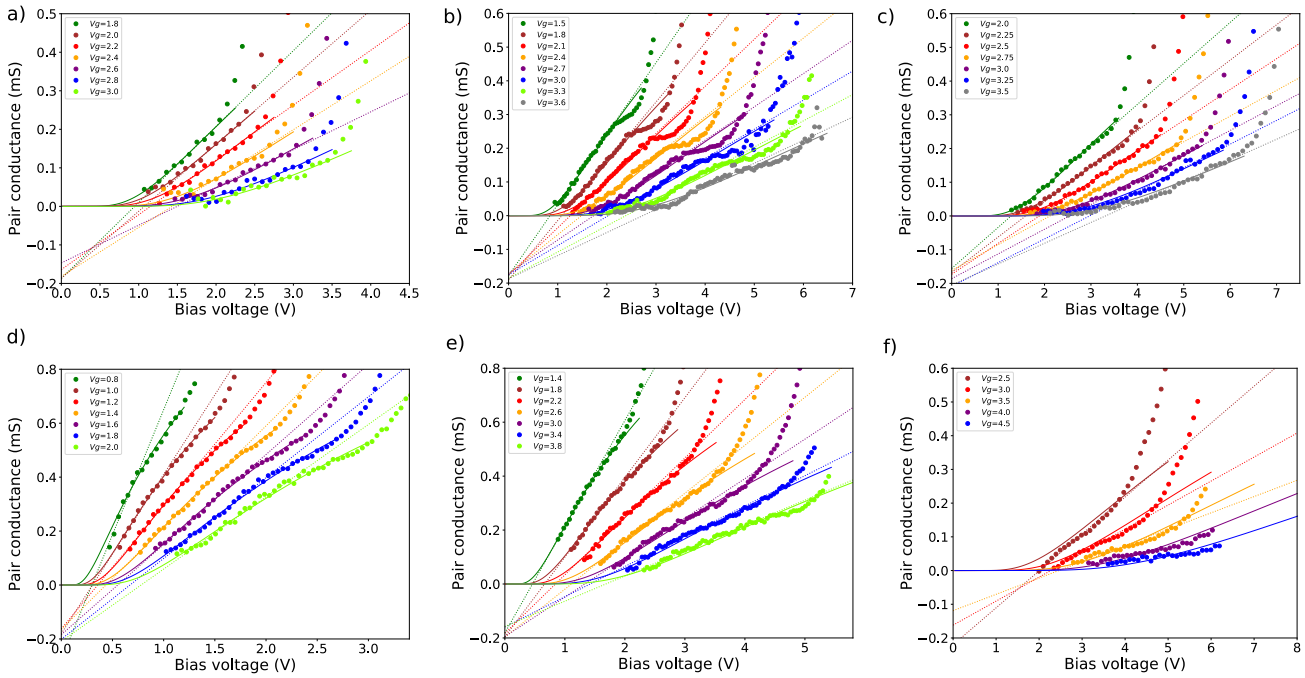

FIG. SI-7: Pair conductance of the device series GrS1 (panel a), GrS2 (panel b), GrS3 (panel c), AuS1 (panel d), AuS2 (panel e) and AuS3 (panel f), obtained from data by subtracting the fitted Klein conductance. Pair conductance can be fitted using the 1d-Schwinger formula (solid lines) over a device-dependent range of bias , highlighting the presence of Schwinger conductance in all devices. The linear extrapolates at zero bias (dotted lines) collapse onto one universal value $G_0 \simeq -0.18$ mS which appears doping- and device-independent. Exact values of the extrapolate can be found in Table SI-1.

GrS3 (panels b and c), the subtraction reveals large Schwinger conductance in sample AuS1 and AuS2 (panels d and e) that was previously obscured by Klein conductance exponential decay. Due to the low value of the Schwinger voltage $V_S \sim 0.5 - 0.7V_g$ in these last two devices, Schwinger pair conductance is visible on a wider bias range before Zener conduction sets in, unveiling the non-linearity of Schwinger conductance at high bias voltages whihc is discussed in the main text (Fig.3d).

The universality of 1d-Schwinger conductance is revealed by the zero-bias linear extrapolate, that gives a unique value $G_0 \simeq 0.18mS$ for all gate voltages and for each of the 6 devices of the series, despite a broad variation of geometrical parameters and electronic mobility. This value closely follows the theoretical expectation $G_0 = 0.186mS$ from Schwinger formula.

Unveiling the visibility of Klein-Schwinger effect is thus an optimization task of the dif-

ferent geometrical parameters; the five devices in this Supplementary Information Section were in fact used to set the optimal visibility properties of the sample GrS3, which is used as a demonstrator in the main text. Prerequisites are a low contact resistance and a very high electronic mobility $\mu \gtrsim 10 m^2 V^{-1} s^{-1}$. The hBN optimal thickness is a trade-off: thin layers cause dielectric breakdown problems and confine V_S below pinch-off, generating an early Schwinger conductance onset that can only be revealed by subtraction. Thick layers shift the Schwinger voltage upwards, eventually above the Zener onset terminating the conductance gap. Klein-Schwinger effect is more easily visible in long channel transistors, due to the Pauli-blocked Zener voltage, and devices with a smaller width favor the Klein-collimation and the appearance of 1d-Schwinger effect.

V. RELATION BETWEEN SCHWINGER VOLTAGE, DOPING AND DIELECTRIC THICKNESS

The variety of devices studied in Section IV allows us to analyze the dependencies between Schwinger voltage, doping and dielectric thickness. Figure 3-c of the main text, and the forelast column of Table SI-1, show the evolution of the ratio between Schwinger voltage and gate voltage V_S/V_g as function of doping n_s for the 6 devices. They consistently show a linear increase with respect to n_s that we can attribute to a Coulomb-repulsion effect from the interactions, with a slope that is device-dependent. This slope is plotted as function of the thickness of the hBN dielectric in Figure SI-8. For the case of devices on graphite backgates, the hBN thickness has been replaced by the sum of t_{hBN} and the graphite thickness t_{Graph}, whose values are given in Table SI-1. This relies on the existence of a Debye length for neutral graphite that we approximate to be the total thickness of the thin graphite flake. The slope exhibits an affine increase as function of hBN thickness, and extrapolates to zero for $t_{hBN} \sim 20nm$. This value is on the order of the Fermi wavelength for typical doping range $n_s = 1 - 2\ 10^{12} cm^{-2}$, which acts as a cut-off for interaction effects.

Let us make the assumption that the Schwinger gap $\Delta_S \sim \mu_s$ which is the only energy scale of the problem. Then, the dielectric thickness t_{hBN} being the only lengthscale of the problem, the doping dependence of the junction length $\Lambda(n_s, t_{hBN})$ can be cast in the form $\frac{\Lambda}{t_{hBN}} = \frac{V_S/E_S}{V_g/E_g} = 4\alpha_g (\frac{\mu_s}{\Delta_S})^2 \frac{V_S}{V_g} \simeq 2.8 \frac{V_S}{V_g}$ where $\alpha_g = \frac{e^2}{4\pi\epsilon_0 \epsilon_{hBN} \hbar v_F} = 0.70$ is the graphene fine structure constant, taking the high-field hBN permittivity $\epsilon_{hBN} \simeq 3.1$ [12].

The measured evolution of $\frac{V_S}{V_g}(t_{hBN}, n_s)$ described in Figure 3-c of the main text and Figure SI-8 can thus be cast into the junction length power expansion $\Lambda \simeq a t_{hBN} + \xi n_s t_{hBN}^2$. Numerical values of Λ are indicated on the right axis in Figure SI-8 and yield $\xi \simeq 4nm$, which corresponds to the typical interaction radius per electron , quantifying the doping-induced dilation of the junction length.

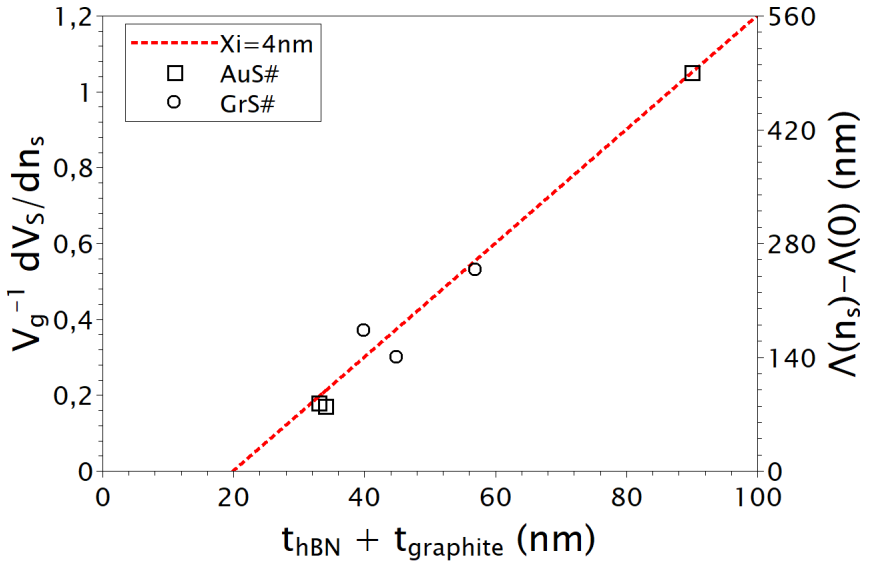

FIG. SI-8: Slope extracted from the linear increase of the ratio $\frac{V_S}{V_g}$ as function of doping n_s (left axis), plotted with respect to the sum of hBN and graphite thicknesses for the 6 devices. Right axis gives the associated value of the junction length $\Lambda(n_s)$. The red dotted line is a linear fit corresponding to $\xi = 4nm$.

The direct consequence of these dependencies is that the 1d-Schwinger conductance becomes hardly visible for devices with thick dielectric such as AuS3, where the Schwinger voltage exceeds the Zener onset voltage even at moderate doping. On the contrary, devices with thin dielectric show an early Schwinger conductance over a large range of doping.

* Electronic address: aurelien.schmitt@phys.ens.fr

† Electronic address: emmanuel.baudin@phys.ens.fr

‡ Electronic address: bernard.placais@phys.ens.fr

[1] C. Itzykson and J.B. Zuber, *Quantum Field Theory*, Dover publications, 2006.

[2] S.M. Sze and K. Ng, *Physics of Semiconductor Devices, Wiley-2007-3rd edition*, Section X.X.X.

[3] M.A. Grado-Caffaro, M. Grado-Caffaro, *Optik* **116**, 299 (2005). *Electrical conductance from the Fowler-Nordheim tunneling*

[4] S.P. Gavrilov. and D.M. Gitman, *Phys. Rev. D* **53**, 7162 (1996). *Vacuum instability in external fields*

[5] A. Shytov, M. Rudnerb, N. Guc, M. Katsnelson, L. Levitov, *Solid State Communications* **149**, 10987 (2009). *Atomic collapse, Lorentz boosts, Klein scattering, and other quantum-relativistic phenomena in graphene*

[6] B. Dora, R. Moessner, *Phys. Rev. B* **81**, 165431 (2010). *Non-linear electric transport in graphene: quantum quench dynamics and the Schwinger mechanism*

[7] S. P. Gavrilov, D. M. Gitman, N. Yokomizo, *Phys. Rev. D* **86**, 125022 (2012). *Dirac fermions in strong electric field and quantum transport in graphene*

[8] N. Vandecasteele, A. Barreiro, M. Lazzeri, A. Bachtold, F. Mauri, *Phys. Rev. B.* **82**, 045416 (2010). *Current-voltage characteristics of graphene devices: Interplay between Zener-Klein tunneling and defects.*

[9] J. Tworzydlo, B. Trauzettel, M. *Phys. Rev. Lett.* **96**, 246802 (2006). *Sub-Poissonian shot noise in graphene*

[10] R. Danneau, F. Wu, M. F. Craciun, S. Russo, M. Y. Tomi, J. Salmilehto, A. F. Morpurgo, P. J. Hakonen, *Phys. Rev. Lett.* **100**, 196802 (2008). *Shot Noise in Ballistic Graphene*

[11] W. Yang, S. Berthou, X. Lu, Q. Wilmart, A. Denis, M. Rosticher, T. Taniguchi, K. Watanabe, G. Fève, J.M. Berroir, G. Zhang, C. Voisin, E. Baudin, B. Plaçais, *Nature Nanotechnol.* **13**, 47 (2018). *A graphene Zener-Klein transistor cooled by a hyperbolic substrate*

[12] A. Pierret, D. Mele, H. Graef, J. Palomo, T. Taniguchi, K. Watanabe, Y. Li, B. Toury, C. Journet, P. Steyer, V. Garnier, A. Loiseau, J-M. Berroir, E. Bocquillon, G. Fève, C. Voisin, E. Baudin, M. Rosticher, B. Plaçais, *Materials Research Express* in

press https://doi.org/10.1088/2053-1591/ac4fe1 (2022). *Dielectric permittivity, conductivity and breakdown field of hexagonal boron nitride*

[13] J. Chaste, E. Pallecchi, P. Morfin, G.Fève, T. Kontos, J.-M. Berroir, P. Hakonen, B. Plaçais, *Appl. Phys. Lett.* **96**, 192103 (2010) *Thermal shot noise in top-gated single carbon nanotube field effect transistors*